https://doi.org/10.5194/egusphere-2025-175
Preprint. Discussion started: 7 February 2025

Building multi-satellite DEM time series for insight into mélange inside large rifts in Antarctica

Menglian Xia[1, 2], Rongxing Li[1, 2], Marco Scaioni[3], Lu An[1, 2], Zhenshi Li[1, 2], Gang Qiao[1, 2]

[1] Center for Spatial Information Science and Sustainable Development, Tongji University, 1239 Siping Road, Shanghai, China, 200092
[2] College of Surveying and Geo-Informatics, Tongji University, 1239 Siping Road, Shanghai, China, 200092
[3] Department of Architecture, Built environment and Construction engineering (ABC), Politecnico di Milano, via Ponzio 31, Milano 20133, Italy

Correspondence to: Rongxing Li (RonLi_282@Hotmail.com)

Abstract. Front calving is a primary mechanism through which Antarctic ice shelves discharge ice mass into the Southern Ocean. It is an important process that influences ice shelf stability and thus, impacts the Antarctic Ice sheet's contribution to global sea level rise. However, there has been a significant gap in large-scale, high-resolution observations of three-dimensional (3D) rift structural changes and mélange dynamics, which hinders our understanding of the role of mélange in ice shelf retreat and mechanisms underlying the weakening of ice shelf stability. We propose an innovative multi-temporal DEM adjustment model (MDAM) that builds a multi-satellite DEM time series from meter-level resolution small DEMs across large Antarctic ice shelves by removing biases, as large as ~6 m in elevation, caused by tides, ice flow dynamics, and observation errors. Using 30 REMA and ZY-3 sub-DEMs, we establish a cross-shelf DEM time series from 2014 to 2021 for the Filchner-Ronne Ice Shelf, the second largest in Antarctica. This unified and integrated DEM series, with an unprecedented submeter elevation accuracy, reveals quantitative 3D structural and mélange features of a ~50 km long rift, including rift lips, flank surface, pre-mélange cavities, and mélange elevations. For the first time, we have observed that while the mélange elevation decreased by 2.1 m from 2014 to 2021, the mélange within the rift experienced a rapid expansion of (7.93±0.03) × 10^9 km^3, or 130%. This expansion is attributed to newly calved shelf ice from rift walls, associated rift widening, and other factors related to rift-mélange interactions. The developed MDAM system and the 3D mélange dynamics analysis methods can be applied for research on ice shelf instability and the future contribution of the Antarctic Ice Sheet to global sea level rise.

1 Introduction

Antarctic Ice Sheet (AIS) has shown a persistent pattern of mass loss and contributed to global sea level rise (GSLR) since the beginning of the satellite earth observation era in 1960s (Jacobs et al., 1992; Allison et al., 2009; Rignot et al., 2019; Smith et al., 2020; Li et al., 2022 and 2023a; Otosaka et al., 2023). Although ice mass of outlet glaciers discharged across the grounding line of AIS is considered as contribution to GSLR, the lost ice mass enters the Southern Ocean from ice shelves mainly through two processes, namely shelf front calving and basal melting, each accounting for ~50% (Depoorter et al., 2013; Liu et al., 2015;

https://doi.org/10.5194/egusphere-2025-175
Preprint. Discussion started: 7 February 2025

Smith et al., 2020; Greene et al., 2022). In contrast to basal melting that occurs on the bottom of ice shelves, calving events are directly observed by using satellite remote sensing in the past decades. Examples of large iceberg calving include a major calving event in the Filchner Ice Shelf in 1986 with an area loss of ~11,500 km^2 (Ferrigno and Gould, 1987), release of an iceberg of ~5,800 km^2 from Larsen C Ice Shelf in 2017 (Larour et al., 2021; Wang et al., 2022), and break out of a part of the "loose tooth" of ~1,680 km^2 from the Amery Ice Shelf in 2019 (Francis et al., 2021; Walker et al., 2021). Although the mechanism of ice shelf caving is not fully understood, calving processes are clearly related to the evolution of rifts as they advect to shelf front and cut icebergs (Joughin and Macayeal, 2005; Hulbe et al., 2010; Walker and Gardner, 2019; Greene et al., 2022). Furthermore, the importance and challenges on studying mélange changes in relation to fractures in both Greenland and Antarctica are fully recognized (Rignot and Macayeal, 1998; Larour et al., 2004 and 2021; Cassotto et al., 2021). However, there has been a lack of large-scale high-resolution observations of 3D rift structural changes and mélange dynamics, which hinders our understanding of the role of mélange in ice shelf retreating and the mechanism of ice shelf stability weakening.

In recent decades, altimetric and stereo mapping satellites have been used to acquire 3D data of earth surface features, which are further used to derive digital elevation models (DEMs) where 3D rift structure and mélange information is inherently available. DEMs from satellite altimetry data at the Antarctic continental scale have relatively lower resolutions, for example, 500 m ICESat (Dimarzio et al., 2007) and ICESat-2 (Shen et al., 2022) DEMs, and 1000 m CryoSat-2 DEM (Slater et al., 2018). Those from optical and SAR satellite stereo mapping data are of higher resolutions and have the potential for geometric modeling and analysis of rifts and mélange features, including 90 m TanDEM-X DEM (Wessel et al., 2021), 30 m ASTER GDEM (Tachikawa et al., 2011), and especially, 2 m REMA DEM (Howat et al., 2019). However, these high-resolution DEMs are derived from relatively narrow swath satellite data and have smaller extents. Thus, the smaller DEMs of different timespans are mosaiced together to cover large rifts and large ice shelves, in which significant discrepancies between individual DEMs are induced by influences of tides, ice flow dynamics, and observation errors (Fig. 1a). Existing methods for co-registration of DEMs are mostly developed based on global fitting and used in a land environment, e.g., a seven-parameter DEM transformation for mountain glacier mass balance estimation (Li et al., 2023b) and a global optimization process for computing three parameters between DEMs using all grid points (Nuth and Kääb, 2011). Furthermore, REMA DEMs are registered to a control data set, such as airborne altimetric data or satellite altimetric data of ICESat and CryoSat-2 (Howat et al., 2019; Shean et al., 2019; Zinck et al., 2023). There is a lack of methods for handling heterogenous offsets between individual DEMs caused by tides, ice flow, rifts, mélange dynamics, and other factors in a dynamic Antarctic ice shelf environment.

https://doi.org/10.5194/egusphere-2025-175
Preprint. Discussion started: 7 February 2025

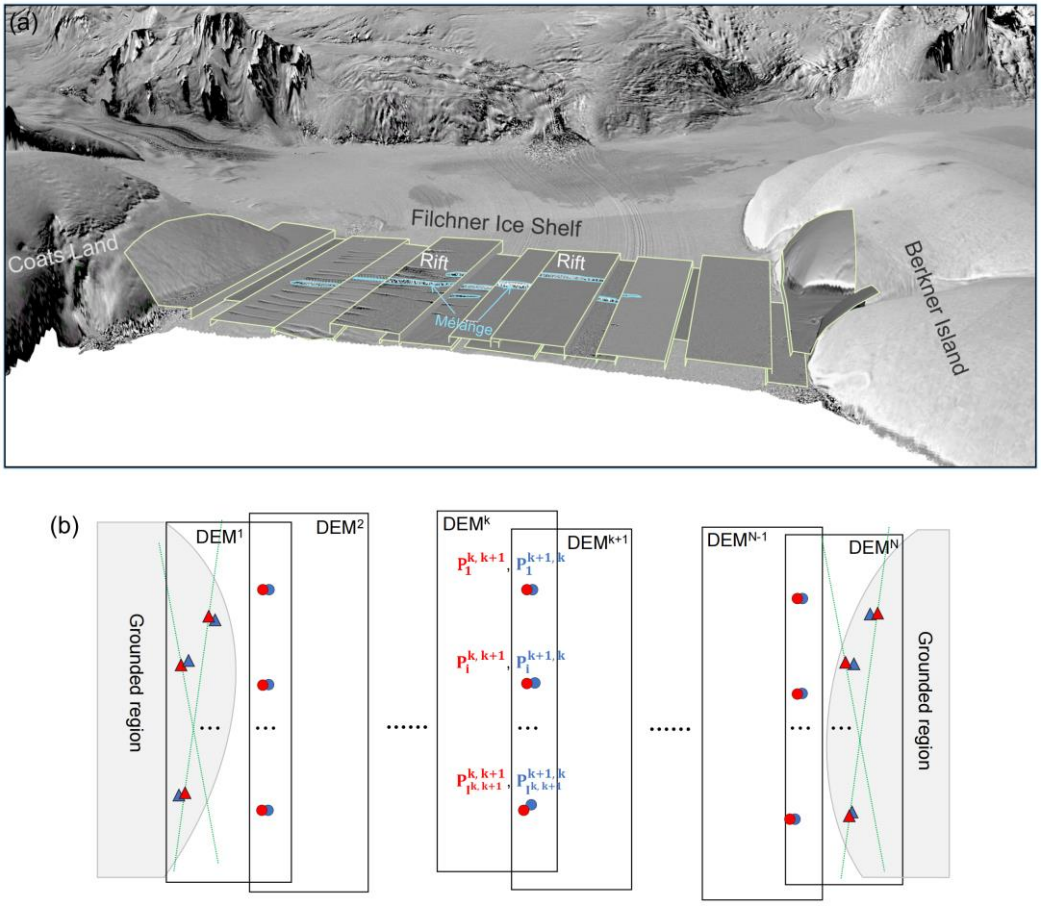

Figure 1. (a) High-resolution small-coverage DEMs are unified and integrated for accurate 3D rift structural and mélange dynamic monitoring in a large Antarctic ice shelf environment (e.g., Filchner Ice Shelf). LIMA mosaic (Bindschadler et al., 2008) is draped on RAMP DEM (Liu et al., 2001) with a vertical exaggeration factor of 40 times. (b) Concept of the MDAM system to connect sub-DEMs across the ice shelf through "tie points" (TP, represented by circles) to create a DEM time series. The "ground control points" (GCP, represented by triangles) are used to fix the combined DEM model to grounded regions at ice shelf margins. The closely located red and blue circles (triangles) are from adjacent sub-DEMs and form corresponding TP (GCP) pairs.

We propose an innovative multi-temporal DEM adjustment model (MDAM) with the purpose to remove biases between adjacent sub-DEMs and to establish a unified and integrated multi-satellite DEM time series with a submeter elevation accuracy. We introduce tie points (TPs) to connect the sub-DEMs and to formulate a DEM time series across a large ice shelf, which is then constrained to grounded regions using ground control points (GCPs). ICESat-2 altimetric data with a centimeter elevation accuracy (Markus et al., 2017) are applied to control the overall geometry of the DEM time series. We develop a data-driven approach to remove large offsets between adjacent sub-DEMs, namely the tide-induced elevation displacements and ice flow-induced horizontal discrepancies, by using a tide model and velocity maps, respectively. The residuals are then minimized in the MDAM system in a least-squares process to obtain the 3D correction parameters of each sub-DEM. The validated MDAM is applied in the Filchner-Ronne Ice Shelf, the second largest in Antarctica, to establish a cross-shelf DEM

https://doi.org/10.5194/egusphere-2025-175
Preprint. Discussion started: 7 February 2025

time series of 2014-2021. We demonstrate the capability of the MDAM for quantitatively characterizing 3D structural and mélange features of a ~50 km long rift, including rift lips, flank surface, pre-mélange cavities, and mélange elevations. Finally, we reveal how the mélange inside the rift changes its elevation and volume dynamically as the rift propagates and advects toward the ice shelf front during the study period.

2 Method

2.1 Multi-temporal DEM adjustment model (MDAM)

As illustrated in Fig. 1b, a set of sub-DEMs (DEM^1, DEM^2, ⋯, DEM^k, ⋯, DEM^{N-1}, DEM^N) are connected through TPs in the overlapping areas between adjacent sub-DEMs. The two sub-DEMs at two shelf margins (DEM^1 and DEM^N) cover grounded regions, while those in between (from DEM^2 to DEM^{N-1}) cover the floating ice of the ice shelf. GCPs are used to fix the entire DEM time series to the grounded regions. They are input into the multi-temporal DEM adjustment model (MDAM) for removing biases between adjacent sub-DEMs (Fig. 2). Initially, relatively large vertical offsets, up to ~6 m, caused by tides are corrected for all sub-DEMs by using a tide model, CATS2008, with an accuracy of ~8 cm (Padman et al., 2008; King et al., 2011). Then we manually select TPs in overlapping areas between sub-DEMs on the floating ice to cover the entire ice shelf. The relatively large horizontal displacements between corresponding TP pairs (Fig. 1b), up to hundreds of meters, induced by ice flow dynamics are compensated by using ITS_LIVE velocity maps (Gardner et al., 2019). At the same time, we tie the GCP locations to satellite altimetry data of ICESat-2. Thereafter, we use the least-squares adjustment method (McGlone et al., 2004) to estimate the known bias corrections of all sub-DEMs by minimizing inconsistencies at TP and GCP pairs, which consist of residuals after the tide and velocity corrections and uncertainty originated from sub-DEM production, including photogrammetric measurement errors and ephemeris data errors (Li, 1998; McGlone et al., 2004; Shean et al., 2019). Finally, the corrected sub-DEMs are applied for 3D analysis and modeling of large rifts and mélange dynamics.

https://doi.org/10.5194/egusphere-2025-175
Preprint. Discussion started: 7 February 2025

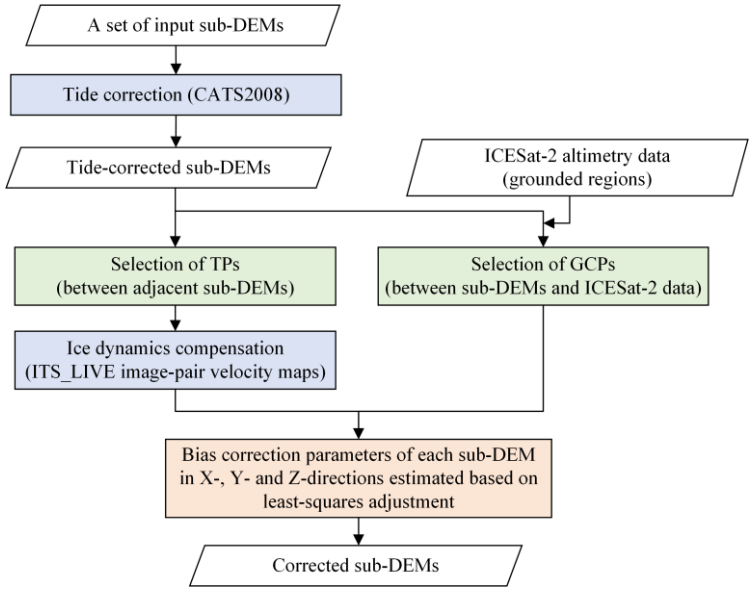

Figure 2. Data processing principle of the multi-temporal DEM adjustment model (MDAM).

For each pair of TPs $P_i^{k,k+1}$ and $P_i^{k+1,k}$ (i=1, ..., $i^{k,k+1}$) (Fig. 1b), we measure 3D coordinates $(X_{P_i}^{\ k}, Y_{P_i}^{\ k}, Z_{P_i}^{\ k})$ from DEM^k and $(X_{P_i}^{\ k+1}, Y_{P_i}^{\ k+1}, Z_{P_i}^{\ k+1})$ from DEM^{k+1}. We define 3D translational parameters of (dX^k, dY^k, dZ^k) as unknowns for bias removal. Thus, we establish the 3D positional relationships at tie point $P_i^{k,k+1}$ between DEM^k and DEM^{k+1} as observation equations for each pair of TPs:

$$\begin{cases} X_{P_i}^{\ k} + dX^k + VelX_i^k * (t^{k+1} - t^k) = X_{P_i}^{\ k+1} + dX^{k+1} + \varepsilon_{x_i}^{\ k} \\ Y_{P_i}^{\ k} + dY^k + VelY_i^k * (t^{k+1} - t^k) = Y_{P_i}^{\ k+1} + dY^{k+1} + \varepsilon_{y_i}^{\ k} \\ Z_{P_i}^{\ k} + dZ^k = Z_{P_i}^{\ k+1} + dZ^{k+1} + \varepsilon_{z_i}^{\ k} \end{cases}, \quad (1)$$

where k = 1, ..., N-1; and i=1, ..., $i^{k,k+1}$. t^k and t^{k+1} are known data acquisition times for DEM^k and DEM^{k+1}. $VelX_i^k$ and $VelY_i^k$ are ice flow speed in X- and Y- directions at the TP given in a velocity map. Similarly, $(dX^{k+1}, dY^{k+1}, dZ^{k+1})$ are unknown bias correction parameters for DEM^{k+1}. $(\varepsilon_{x_i}^{\ k}, \varepsilon_{y_i}^{\ k}, \varepsilon_{z_i}^{\ k})$ represent residuals of the observation equations

In the similar way, observation equations for ground control point $P_{GCP_i}^{\ k}$ are given as:

$$\begin{cases} X_{GCP_i}^{\ k} + dX^k = X_{P_i}^{\ GCP,k} + \varepsilon_{x_i}^{\ GCP,k} \\ Y_{GCP_i}^{\ k} + dY^k = Y_{P_i}^{\ GCP,k} + \varepsilon_{y_i}^{\ GCP,k} \\ Z_{GCP_i}^{\ k} + dZ^k = Z_{P_i}^{\ GCP,k} + \varepsilon_{z_i}^{\ GCP,k} \end{cases} \quad (2)$$

where k = 1 and N; and i=1, ..., $i^{GPC,k}$. $(X_{GCP_i}^{\ k}, Y_{GCP_i}^{\ k}, Z_{GCP_i}^{\ k})$ are 3D coordinates measured at the GCP from DEM^k. $(X_{P_i}^{\ GCP,k}, Y_{P_i}^{\ GCP,k}, Z_{P_i}^{\ GCP,k})$ are 3D coordinates at the same point from the control data set (e.g., ICESat-2). Furthermore, it is noticed that in the study area, elevation disagreements between adjacent REMA DEMs present a linear trend in the Y-direction (mainly ice flow direction). Thus, we use a linear term of $a_o^k + a_1^k\, Y_{OL_i}^{\ k}$ to replace dZ^k in Eqs. (1) and (2). Here, a_o^k

https://doi.org/10.5194/egusphere-2025-175
Preprint. Discussion started: 7 February 2025

and a_1^k are coefficients as unknowns, and ${Y_{OL_i}}^k$ is the Y coordinate defined in the local central coordinate system in the overlapping region between, with the origin defined at the center of the overlapping area.

Eqs. (1) and (2) are combined and populated with all TPs and GCPs of the sub-DEMS. They are further formulated as an observation equation system in a matrix form. Finally, the unknowns, namely bias correction parameters (dX^k, dY^k, a_o^k, and a_1^k) $(k = 1, .., N)$, are solved by an optimization procedure using the least-squares principle (McGlone et al., 2004). Uncertainties of the estimated bias correction parameters are computed through an error propagation within the optimization procedure.

2.2 Implementation

2.2.1 Site and data

The proposed MDAM model is validated and applied in the Filchner Ice Shelf, one of the dual ice shelves of Filchner-Ronne Ice Shelf that is the second largest in Antarctica (Fig. 3). Berkner Island and Coats Land are located at western and eastern margins of the ice shelf, respectively. The largest calving event recorded for this ice shelf, with an area loss of 11500 km^2, occurred in 1986 due to a rapid propagation of a prominent rift known as “Grand Chasm” (Ferrigno and Gould, 1987), producing three giant icebergs that greatly impacted the circulation and hydrography in the nearby ice shelf-ocean system (Grosfeld et al., 2001). Recently, two large rifts, T1 and T2, are detected in a Landsat satellite image in 1996 and an ARGON satellite image in 1963, respectively (Li et al., 2017; Walker and Gardner, 2019; Lv et al., 2022). These rifts have a combined length of ~100 km and exhibit a similar propagation pattern as Grand Chasm. To study their 3D evolution and mélange dynamics inside the rifts is important for assessment of the ice shelf instability and forecasting of the next major calving event. In this study we focus on rift T1 because of its dynamic propagation characteristics and more matured mélange.

https://doi.org/10.5194/egusphere-2025-175
Preprint. Discussion started: 7 February 2025

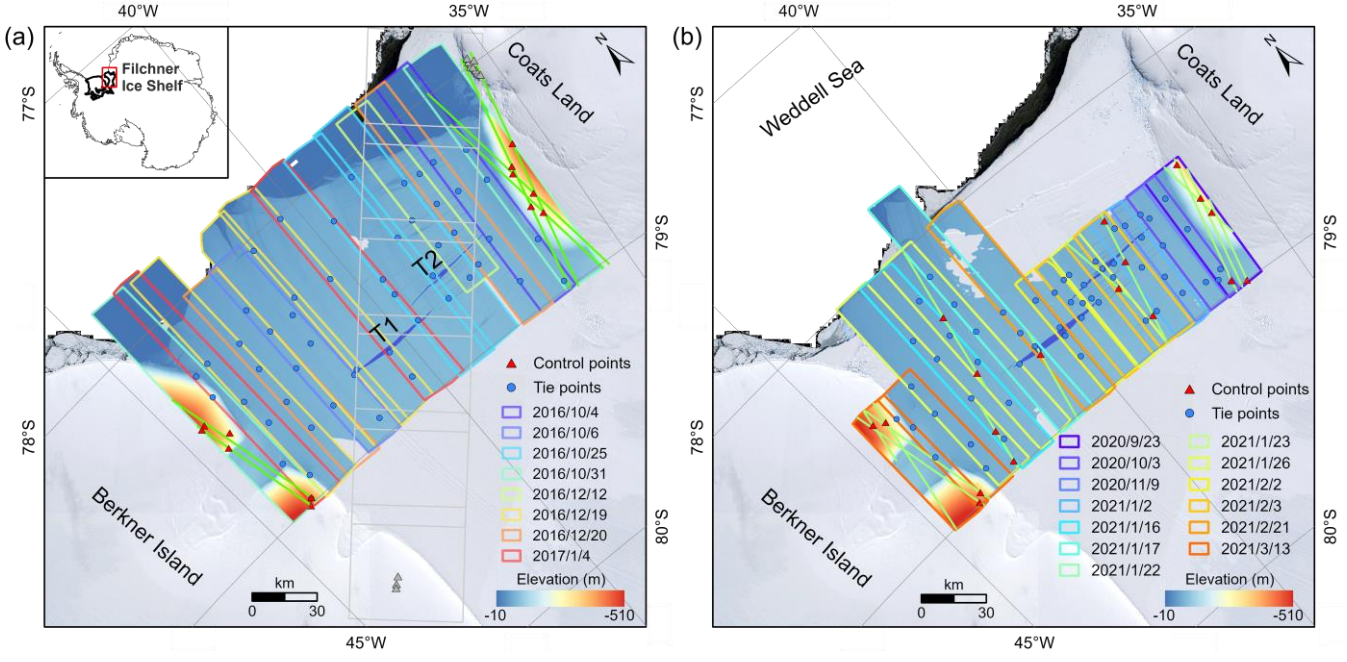

Figure 3. The Filchner Ice Shelf used as a validation and application site for the MDAM system. Colored boxes are REMA DEM coverages. Green lines at Berkner Island and Coats Land are ICESat-2 tracks. Blue circles are TPs and red triangles are GCPs. (a) REMA DEMs of 2016–2017, ZY-3 DEM of 2014 (light gray lines), and rifts T1 and T2. (b) REMA DEMs of 2020–2021. Background elevation information is from REMA DEM (Howat et al., 2019).

The sub-DEMs used in this study are generated from two data sources, namely stereo satellite images of WorldView (Anderson and Marchisio, 2012) and Ziyuan-3 (ZY-3) (Wang et al., 2014), both formed by the along-track stereo mechanism (Li, 1998). REMA DEMs are available for the entire Antarctica and are produced from WorldView images using an open-source automatic photogrammetric processing software system, Surface Extraction from TIN-based Searchspace Minimization (SETSM) (Noh and Howat, 2015). The WorldView data set includes WorldView-1, -2 and, -3, and GeoEye-1 images with a small swath of 13.1–17.6 km and a high resolution of 0.3 m–0.5 m (Howat et al., 2019). Thus, each derived REMA DEM provides a high level of ice surface details, but with a relatively small extent, resulting in difficulties in covering large rifts or the entire ice shelf. More specifically, we use REMA DEM strips of 2016-2017 (Fig. 3a) and 2020-2021 (Fig. 3b) with a grid spacing of 2 m. On the other hand, ZY-3, launched in 2012, is the first Chinese high-resolution natural resource mapping satellite (Wang et al., 2014). It is equipped with a three-line mapping system that forms quasi-real-time along-track stereo image pairs using fore (3.5 m), nadir (2.1 m), and aft (3.5 m) views. The fore and aft combination has a large intersection angle of 47°, facilitating a high elevation accuracy for DEM generation. Its wide swath of ~52 km ensures a complete coverage of large rifts, such as T1 and T2 (Fig. 3a). The ZY-3 DEM used in this study has a time tag of February 28, 2014 and a grid spacing of 5 m. It has a relatively narrow strip because of cloud coverage, but it covers both T1 and T2. The DEM is registered to the ICESat-2 altimetry data and has an elevation accuracy of 0.3 m.

We use elevation points of the ICESat-2 ATL 6 data from 2019 to 2021 (Markus et al., 2017) to register the ZY-3 DEM. The

https://doi.org/10.5194/egusphere-2025-175
Preprint. Discussion started: 7 February 2025

GCPs are also selected on or close to ICESat-2 ATL 6 elevation points to establish a unified reference system. The ICESat-2 data are also used for validation of the bias-corrected DEM time series. Along each of the six beam tracks, ICESat-2 ATL 6 data provide aggregated elevation points with a 20 m spacing and a revisit cycle of 91 days. Field validation studies have demonstrated that the ICESat-2 data reached an elevation accuracy within 2–4 cm in Antarctica (Brunt et al., 2019; Magruder et al., 2020; Li et al., 2021).

2.2.2 Implementation aspects

GCP Selection

Selection of high quality GCPs is of great importance to the accuracy of the entire DEM time series. We choose GCPs on the grounded regions at both margins of the ice shelf (Fig. 1b) with considerations of stability, low ice velocity, and local peaks (Feng et al., 2022). Meanwhile, the GCPs are also chosen to be on or close to the ICESat-2 ATL 6 points from which their 3D coordinates can be measured. Despite the absence of outcrops and blue ice in the grounded regions of this study, we are able to identify relatively stable features for GCP selection, aided by multisource data, e.g., REMA DEMs, ICESat-2 data, ice flow velocity maps (Rignot et al., 2011), and bed topography (Morlighem et al., 2020).

Fig. 4 illustrates an example of GCP selection on the ice surface of Coats Land. Within a local area we drape a shaded relief map and a velocity map (Rignot et al., 2011) on the REMA DEM to make sure that a GCP candidate is selected not on a steep slope (< 5°) and with a low ice flow speed (< 10 m y^{-1}) (Fig. 4a and 4b). The candidate is approximately localized at a local peak (red dot). In a close-up view (Fig. 4c and 4d), an ICESat-2 elevation profile (blue line) is further used to finalize the GCP position by adjusting the candidate position to the local maximum of the terrain (red cross). Finally, 3D coordinates of the GCP are measured on the ICESat-2 profile as knowns ($X_{P_i}^{GCP,N}$, $Y_{P_i}^{GCP,N}$, $Z_{P_i}^{GCP,N}$) and from the sub-DEM as observations ($X_{GCP_i}^{N}$, $Y_{GCP_i}^{N}$, $Z_{GCP_i}^{N}$) that are used in Eq. (2).

https://doi.org/10.5194/egusphere-2025-175
Preprint. Discussion started: 7 February 2025

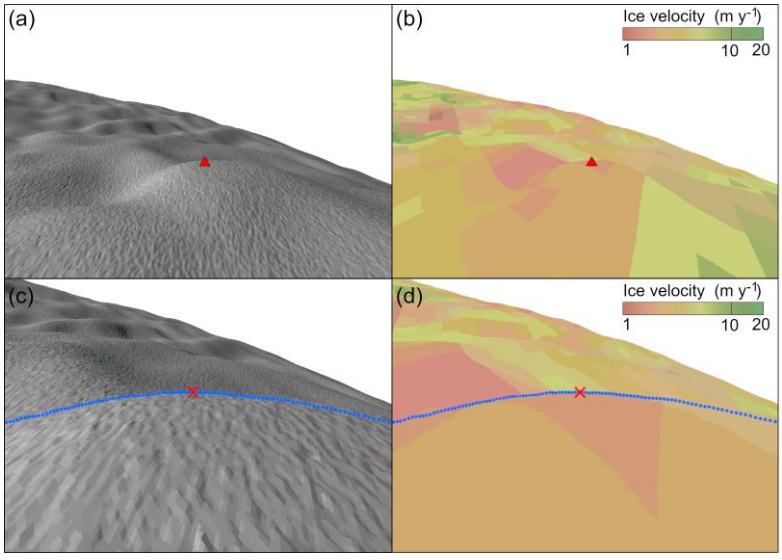

Figure 4. Local 3D view for GCP candidate (red dot) selection: shaded relief map (a) and velocity map (b) draped on the REMA DEM. 3D close-up view for GCP finalization (red cross): local maximum selected with help of the ICESat-2 elevation profile (blue line) (c) and velocity map (d).

TP Selection

The key consideration for TP selection is to choose features that are identifiable on both adjacent sub-DEMs and unchanged during the time interval between the acquisitions of the sub-DEMs. Further specific rules are followed: (1) if applicable, TPs be selected at distinct features, such as crevasses, rifts, and other relatively "stable" ice surface features; (2) elevated locations are preferred to avoid influences of shadows casted by different lighting conditions and obstacles in 3D visualization; and (3) TPs be approximately evenly distributed in the overlapping area. For example, to select a TP candidate on a rift lip, two shaded relief maps are produced from the adjacent sub-DEMs and used for 3D visualization (Fig. 5a and 5b) to check whether the feature (orange and blue dots in Fig. 5) is changed during the time interval between the two sub-DEMs. The TP is finalized (red cross) by a verification using a 3D Landsat image view with a different illumination geometry (Fig. 5c). Fig. 5d–5f shows another example of TP selection on a snow bridge that is formed by an ice surface process when snow is blown into a crevasse and rift and accumulated about tens of meters above the shelf surface (Williams et al., 2014; Thompson et al., 2020). Similarly, Fig. 5d and 5e show the 3D views from shaded relief maps with lower elevation angles produced from adjacent sub-DEMs. After a verification using a Landsat image (Fig. 5f), the peak of the snow bridge is defined as the TP. In both cases, 3D coordinates $(X_{P_i}^{\ k}, Y_{P_i}^{\ k}, Z_{P_i}^{\ k})$ and $(X_{P_i}^{\ k+1}, Y_{P_i}^{\ k+1}, Z_{P_i}^{\ k+1})$ are measured and used in Eq. (1).

https://doi.org/10.5194/egusphere-2025-175
Preprint. Discussion started: 7 February 2025

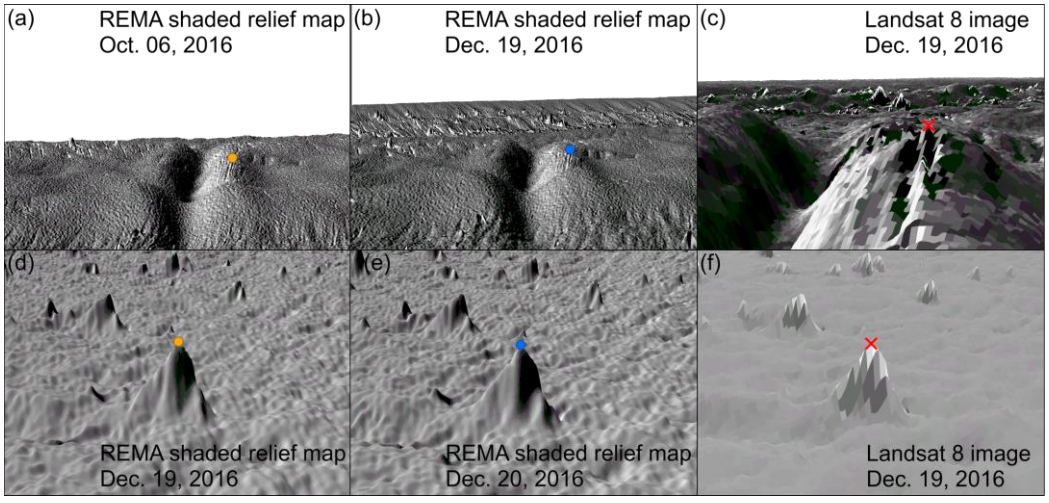

Figure 5. TP selection on rift lip: 3D views from two shaded relief maps of adjacent REMA DEMs (a) and (b), and verification using a 3D Landsat image view (c). TP selection on snow bridge: 3D views from two shaded relief maps of adjacent REMA DEMs (d) and (e); verification using a 3D Landsat image view.

3 Results

3.1 Bias correction and adjusted DEM time series

The REMA DEMs of 2016-2017 consists of 14 sub-DEMs that cover the entire front part of Filchner Ice Shelf (Fig. 3a). We use 12 GCPs that are measured by using ICESat-2 data to tie the connected DEMs to the grounded regions of Berkner Island and Coats Land where the average ice flow speed at the GCPs is ~8 m y^{-1}. In total 51 TPs are used to connect the sub-DEMs on the flowing ice of the ice shelf, with 3-4 evenly distributed TPs in each overlapping area. Horizontal displacements at the TPs caused by the ice flow are in average ~90 m and are corrected by using the velocity map (Gardner et al., 2019). We establish the observation equations in Eqs. (1) and (2) using different weights. The weights for TPs are computed as inverse distances from the TPs to the nearest GCPs on grounded regions. Hence, the weights for GCPs are set to 1. Those TPs that are farther away from the grounded regions have smaller weights.

Table 1. Bias corrections (dX^k, dY^k, dZ^k) estimated for 14 sub-DEMs, ordered from Berkner Island to Coats Land, for the REMA DEMs of 2016-2017.

DEM^k	$dX^k \pm \sigma_{dX}$ (m)	$dY^k \pm \sigma_{dY}$ (m)	$dZ^k \pm \sigma_{dZ}$ (m)
1	4.58±1.42	-4.20±1.45	3.15±0.07
2	8.68±2.58	-2.38±2.85	-1.15±0.13
3	6.24±3.14	-7.57±4.05	-1.08±0.18
4	7.79±3.53	-5.33±5.11	5.91±0.24
5	-5.28±3.80	-9.77±6.00	-5.76±0.29

https://doi.org/10.5194/egusphere-2025-175
Preprint. Discussion started: 7 February 2025

6	1.55±4.03	2.31±6.69	4.38±0.36
7	3.07±4.12	0.19±7.18	-0.27±0.43
8	-0.24±4.10	1.07±7.12	-1.07±0.38
9	-1.36±4.00	9.98±6.69	-1.98±0.33
10	-2.03±4.07	11.61±6.00	-2.33±0.30
11	-4.00±4.07	13.71±5.11	3.11±0.24
12	-0.75±3.83	4.46±2.85	2.65±0.19
13	0.69±3.57	1.69±1.45	-2.40±0.16
14	-1.91±3.20	0.00±0.00	-0.48±0.09

The proposed MDAM system estimates the bias corrections (dX^k, dY^k, dZ^k) for all sub-DEM DEM^k (k = *1, 2, ..., 14*) (Table 1) through the least-squares procedure where their uncertainties are provided in the covariance matrix (McGlone et al., 2004). As illustrated in Fig. 6, uncertainties of the corrections in both horizontal and elevation directions are effectively controlled for sub-DEMs close to grounded regions in Berkner Island and Coats Land through GCPs, leaving those in the middle section of the ice shelf relatively higher. The average uncertainty of the elevation corrections is 0.24 m, with the maximum of 0.43 m.

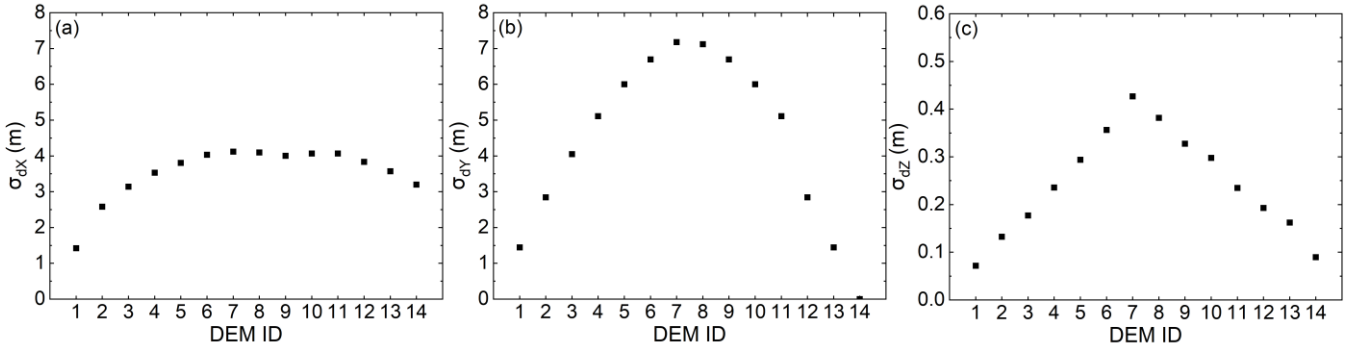

Figure 6. Illustration of uncertainties of the estimated bias corrections (dX^k, dY^k, dZ^k) in Table (1).

These corrections are then applied to each sub-DEMs to produce the bias-corrected REMA DEMs of 2016-2017. The effectiveness of the MDAM system is clearly demonstrated by a dramatic reduction of the elevation offset between adjacent sub-DEMs at the 51 TPs and 12 GCPs (Fig. 7), in average, from 3.72 m before bias-correction (black arrows) to 0.14 m thereafter (red arrows, also called residuals). Residuals vary from 0.01 m to 0.51 m.

https://doi.org/10.5194/egusphere-2025-175
Preprint. Discussion started: 7 February 2025

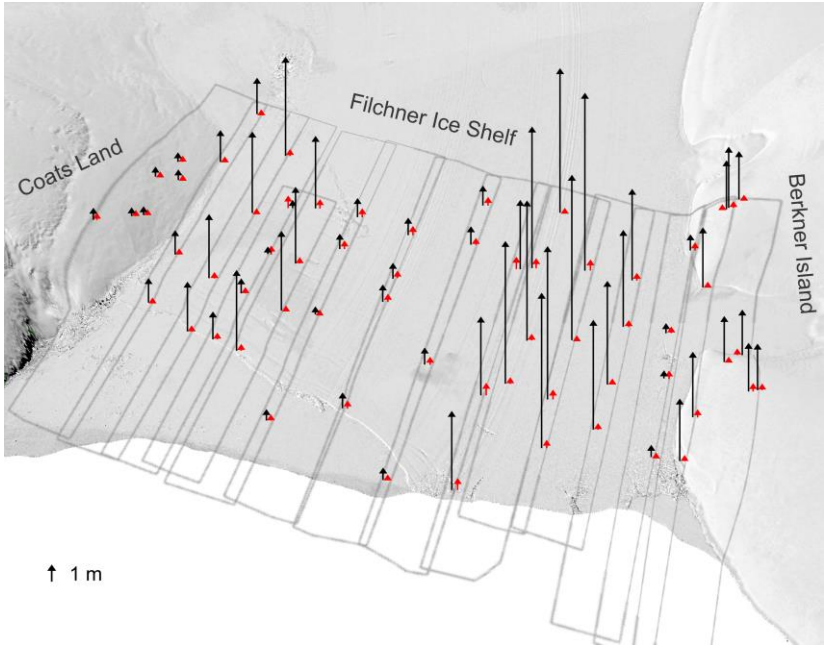

Figure 7. Elevation offsets between adjacent sub-DEMs at TPs and GCPs in the REMA DEMs of 2016-2017 before bias-correction (black arrows, tide and ice velocity compensated) and thereafter (red arrows).

We process the second set of REMA DEMs of 2020-2021 (Fig. 3b) in the same way and establish the bias-corrected DEMs with an average uncertainty of 0.18 m for the elevation bias corrections of dZ^k (Table A1), estimated in the least-squares process. In addition, the ZY-3 DEM of 2014 is reconstructed as a cross-ice-shelf DEM and does not need to go through this bias-correction process. The DEM is co-registered to the ICESat-2 ATL06 data of 2019 with an elevation accuracy of 0.30 m.

https://doi.org/10.5194/egusphere-2025-175
Preprint. Discussion started: 7 February 2025

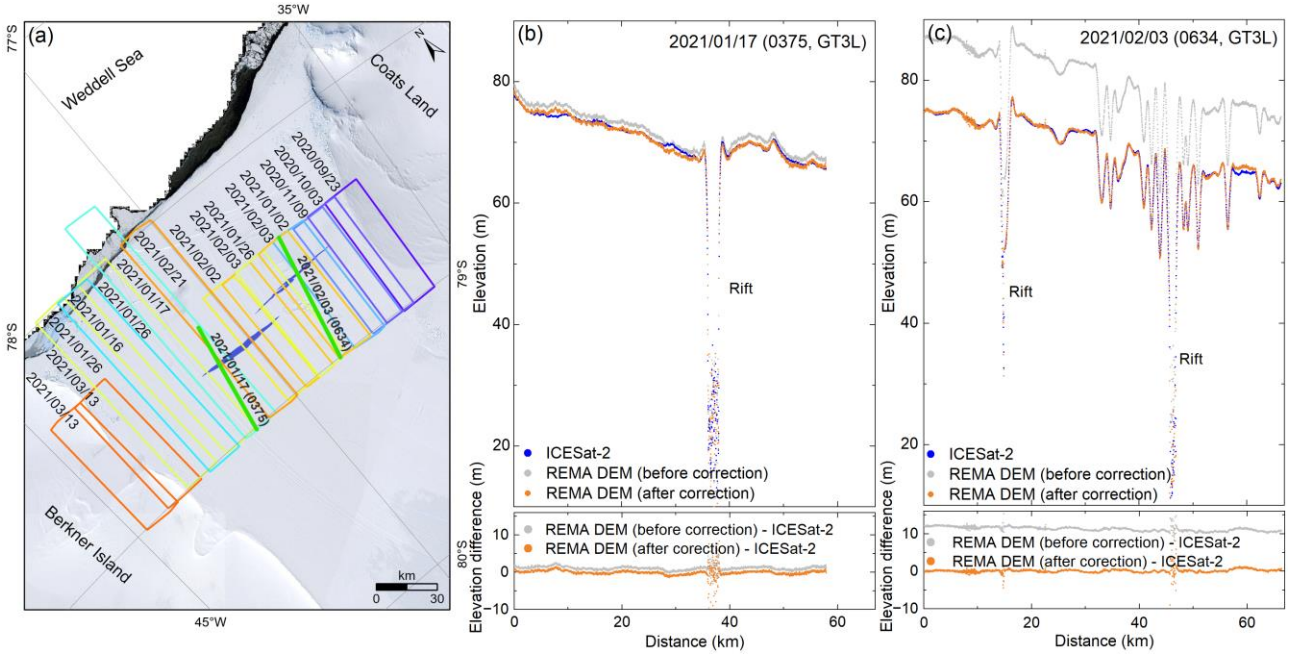

Figure 8. Verification of bias-corrected REMA DEMs of 2020-2021: (a) data acquisition times and footprints of REMA DEMs in different colors, and times and two ground tracks of ICESat-2 data in green color; (b) and (c) elevation profiles of REMA DEMs of 2020–2021 prior to (gray) and post (orange) bias-correction, and ICESat-2 ATL06 data of 2021 (blue), with their corresponding differences at bottom.

To validate the bias-correction results using an external dataset, we directly compare the bias-corrected REMA DEMs of 2020-2021 with two tracks of ICESat-2 ATL06 data acquired from January to February 2021 (green lines in Fig. 8a). The ICESat-2 data set is chosen because of its high elevation accuracy and along-track point density. Furthermore, we select two tracks of the ICESat-2 data that were acquired on the same times (within one day) as the REMA sub-DEMs to avoid displacements caused by the shelf ice advection and internal mélange changes. The timespans of other two sets of DEMs, REMA DEMs 0f 2016-2017 and ZY-3 DEM, fall outside the ICESat-2 temporal coverage. Along Orbit 0735 Ground track GT3L, REMA DEM points prior to bias correction (gray) are relatively close to the ICESat-2 ATL 6 elevation points (blue points), with a smaller average difference of 1.07 m (Fig. 8b). However, the average difference of 11.23 m along Orbit 0634 Ground track GT3L is significantly larger (Fig. 8c). After bias-corrections, the differences are effectively controlled within 0.09 m on these two tracks and 0.18 m on mélange top.

3.2 3D mélange dynamics from 2014-2021

https://doi.org/10.5194/egusphere-2025-175
Preprint. Discussion started: 7 February 2025

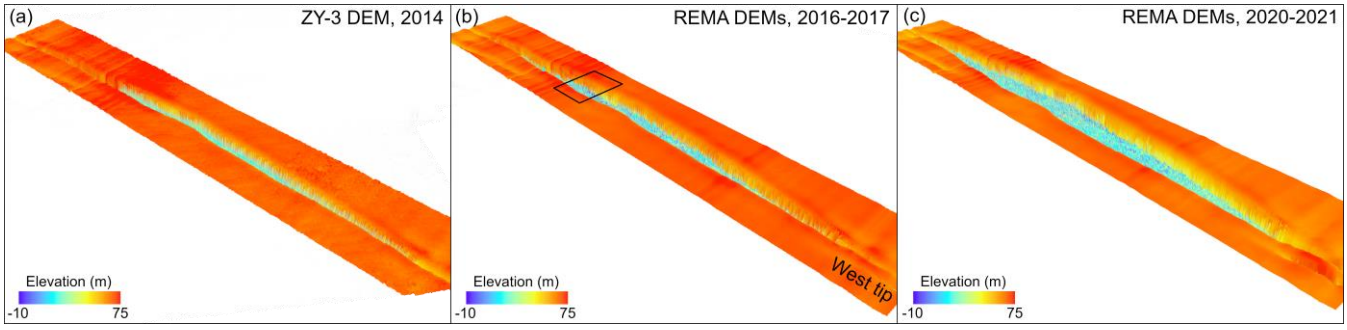

Figure 9. Multi-satellite DEM time series of the large rift T1 on Filchner Ice Shelf from 2014 to 2021: (a) reconstructed ZY-3 DEM of 2014, (b) bias-corrected REMA DEMs of 2016-2017, and (c) bias-corrected REMA DEMs of 2020-2021. The box in (b) indicates a section of the rift where details of 3D structure and mélange are presented in Fig. 10.

Based on the registered ZY-3 DEM of 2014 and bias-corrected sub-DEMs of REMA DEMs of 2016-2017 and 2020-2021, we establish a multi-satellite DEM time series of the large rift, T1, from 2014 to 2021 (Fig. 9, Table A2). Each of these periodical unified and integrated DEMs presents the unprecedented 3D structural information of this ~50 km long rift. The unique DEM time series allows us to exploit 3D structure characteristics, including ice surface flank, rift lips, and mélange top and thickness (Fig. 10c). For the first time, we can accurately compute mélange elevation and volume changes within the entire rift as it propagates and advects towards the shelf front during the period of 2014-2021 (Fig. 10d). To quantify 3D dynamic mélange changes within T1, we define a transect system based on the ZY-3 DEM of 2014 where transects are spaced at an interval of 1 km along the rift centerline from the west tip to the east tip, which is also applied to the bias-corrected REMA DEMs of 2016-2017 and 2020-2021.

https://doi.org/10.5194/egusphere-2025-175
Preprint. Discussion started: 7 February 2025

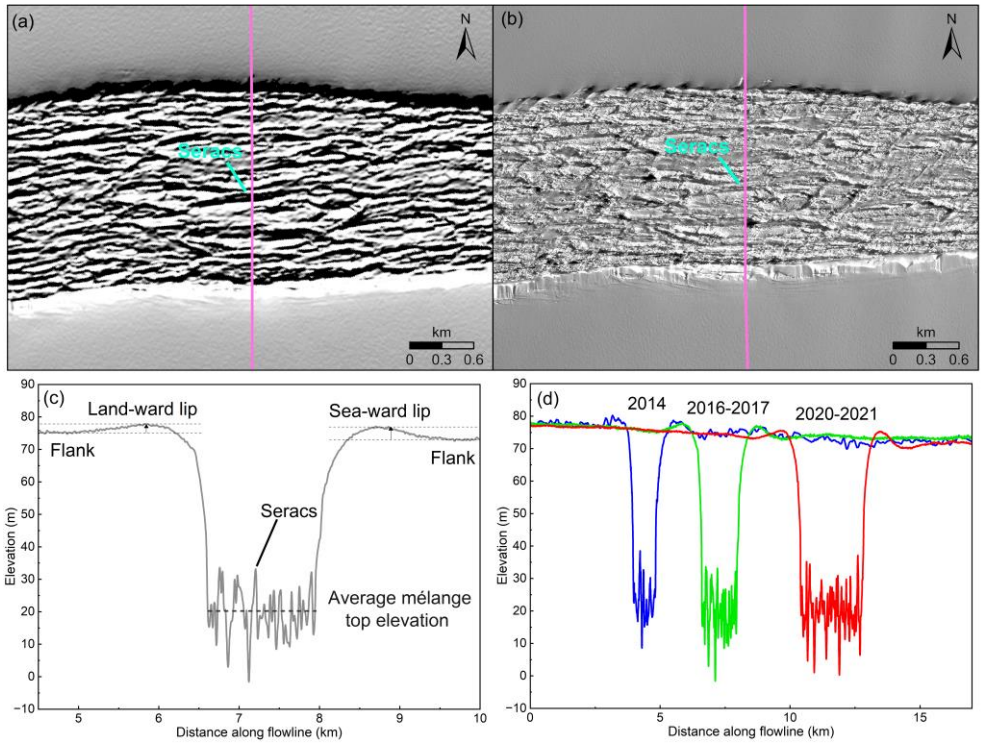

Figure 10. 3D sectional structure and mélange in T1: (a) shaded relief map of a section of REMA DEMs of 2016-2017 (January 4, 2017) indicated by the box in Fig. 9b; (b) WorldView image (0.5 m resolution) of February 25, 2016; (c) elevation profile along the pink line in (a) and (b), and 3D rift and mélange structure parameters; and (d) rift and mélange changes along the profile from 2014 to 2021 (February 28, 2014 in blue, January 4, 2017 in green, and February 2, 2021 in red). Elevation displayed in (a) is exaggerated by 10 times.

Rift T1 has a length of 4713.17 km and a maximum width of 1,456.65 m measured on the ZY-3 DEM of 2014. Based on the bias-corrected DEM time series from 2014 to 2021 (Fig. 9), we found that the rift propagated consistently during the period, resulting in an accelerated widening by 646.83 m (226.95 m y^{-1}) during 2014-2017 and 1,108.71 m (268.36 m y^{-1}) during 2016-2021. Correspondingly, the rift has lengthened by 2393.17 m (839.68 m y^{-1}) during 2014-2017, but only 1,082.83 m (262.10 m y^{-1}) during 2016-2021. Based on the REMA DEMs of 2016-2017, the rift lip on the sea-ward side is mostly higher than that on the landward side in the middle section of the rift (Table A3), with an average difference of 0.60 m from all transects and the largest difference of 3.08 m at the position located about ~35 km from the west tip. This phenomenon precisely measured from the bias-corrected sub-DEMs of the large rift T1 is consistent with the results for some rifts on other Antarctic ice shelves presented in Walker et al. (2019).

https://doi.org/10.5194/egusphere-2025-175
Preprint. Discussion started: 7 February 2025

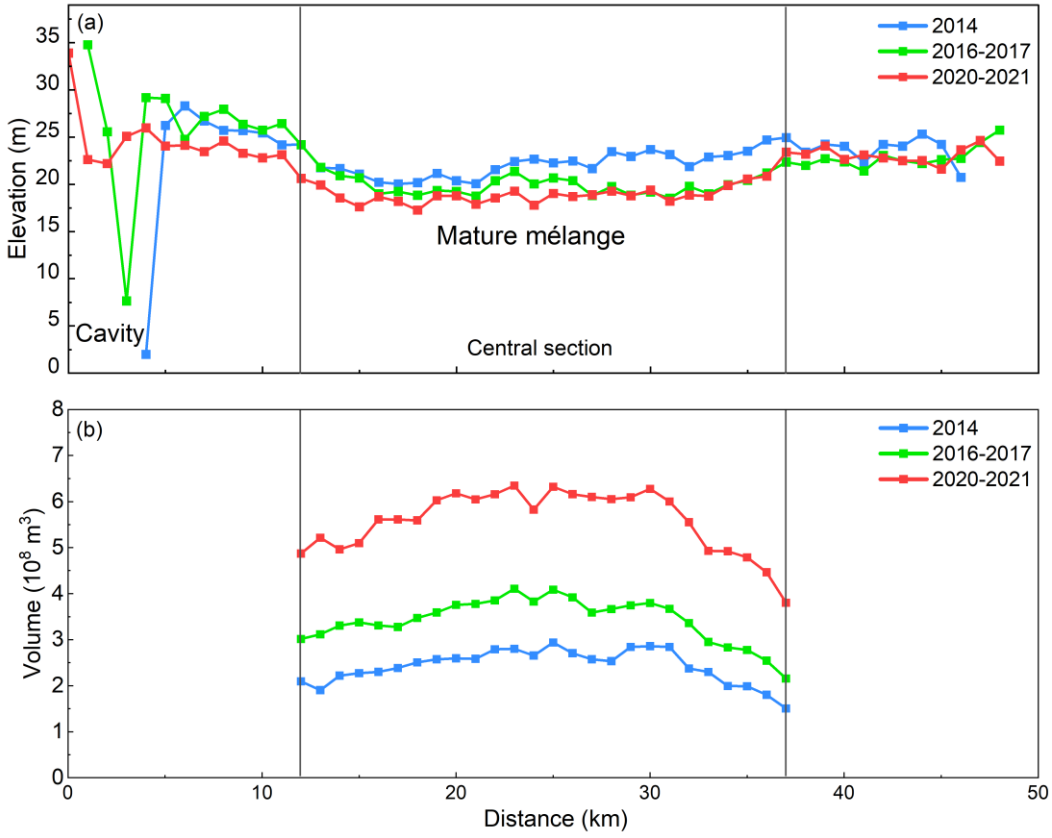

Figure 11. Elevation (a) and volume (b) of ice mélange inside the rift T1 from the multi-satellite DEM series from 2014 to 2021. Average elevation and volume of each transect that are separated every 1 km along the rift centerline are illustrated from west tip to east tip.

Fig. 11a illustrates the average mélange top elevations inside T1 from the YZ-3 DEM of 2014, REMA DEMs of 2016-2017 and REMA DEMs of 2020-2021. Mélange top elevation profiles in the central section of the rift are relatively flat where distinct linear features, called Seracs in Neuburg et al. (1959) and Alley et al. (2023), appear floating with a dominant orientation parallel to the rift centerline in both shaded relief map of DEM (Fig. 10a) and WorldView satellite image (Fig. 10b). We believe that this section of the rift cuts through the ice shelf and call the mélange "mature mélange". In contrast, the mélange in the sections close to both rift tips has relatively rugged surface. More specifically, cavities are found close to the west tip (Fig. 11a), which are verified in ZY-3 stereo images (Fig. A1). They are initially as deep as 24.27 m in the ZY-3 DEM of 2014. As the rift propagates in both length and width, new shelf ice in this section breaks apart from rift walls and fills in the cavities, resulting in a 5.66 m reduction in the cavity depth in the bias-corrected REMA DEM of 2016-2017 (Fig. 11a), and finally, disappearing during 2020-2021. During this process, we believe that the rift in this section cuts the ice shelf deeper and deeper, and the premature mélange becomes gradually mature.

The established DEM time series unveils an overall decrease of 2.1 ± 0.38 m (excluding cavity), at a rate of -0.30 ± 0.05 m y^{-1}, in mélange elevation inside T1 from 2014 to 2021 (between blue and red lines in Fig. 11a). To compute the corresponding

https://doi.org/10.5194/egusphere-2025-175
Preprint. Discussion started: 7 February 2025

volumetric change from this elevation change of the mélange, we apply the hydrostatic equilibrium principle to obtain the unknown thickness H of the mélange in each transect (Fricker et al., 2005):

$$H = \frac{\rho_{water}}{\rho_{water} - \rho_{mélange}}(h - h_{sea}) \quad (3)$$

where h is the average mélange elevation along the transect and h_{sea} is the average sea level (-15.2 m) estimated from the ICESat-2 altimetry data within a range of ~10 km from the ice shelf front from March 2019 to December 2021 during which the ICESat-2 data become stable after the initial stage of the mission (Magruder et al., 2021). ρ_{water} and $\rho_{mélange}$ are densities of seawater and mélange (1,028 kg m^{-3} and 865 kg m^{-3}), respectively (King, 1994; Fricker et al., 2005; Adusumilli et al., 2020). We calculate the overall mélange volume inside the rift by an integration of the sub-volume of each transect (Σ H × *transect interval* × *sampling interval along transect*) in the mature mélange section. Our results indicate that despite the significant decrease in mélange elevation from 2014 to 2021 (Fig. 11a), the inferred periodical mélange volumes reveal a rapid expansion of the mélange by (7.93±0.03) × 10^9 km^3, or 130%, during the period (Fig. 11b), mainly attributed to newly calved shelf ice from rift walls, associated rift widening, and other rift-mélange interaction factors.

4 Conclusion

We have developed an innovative multi-temporal DEM adjustment model (MDAM). This system successfully removed biases, as large as ~6 m in elevation, between 50 sub-DEMs across the Filchner Ice Shelf in East Antarctica. The bias-corrected multi-satellite DEM time series has been validated by using the ICESat-2 altimetry data and achieved an accuracy of 0.09 m. Using this unified and integrated high-resolution DEM time series from 2014 to 2021, for the first time, we unveiled the 3D structural and mélange parameters of the ~50 km long rift T1, including the rift lip height, pre-mélange cavity, and mélange elevation. Our findings indicate that while the mélange elevation decreased by 2.1±0.38 m from 2014 to 2021, the mélange within the rift experienced a rapid expansion by (7.93±0.03) × 10^9 km^3, or 130%, during the period. This expansion is attributed to newly calved shelf ice from rift walls, associated rift widening, and other rift-mélange interaction factors. These new insights into 3D mélange dynamics are important for studying the mechanisms and the role of mélange in rift propagation. The developed MDAM system can be applied for research on ice shelf instability and future contribution of the AIS to global sea level rise.

Appendix A

https://doi.org/10.5194/egusphere-2025-175
Preprint. Discussion started: 7 February 2025

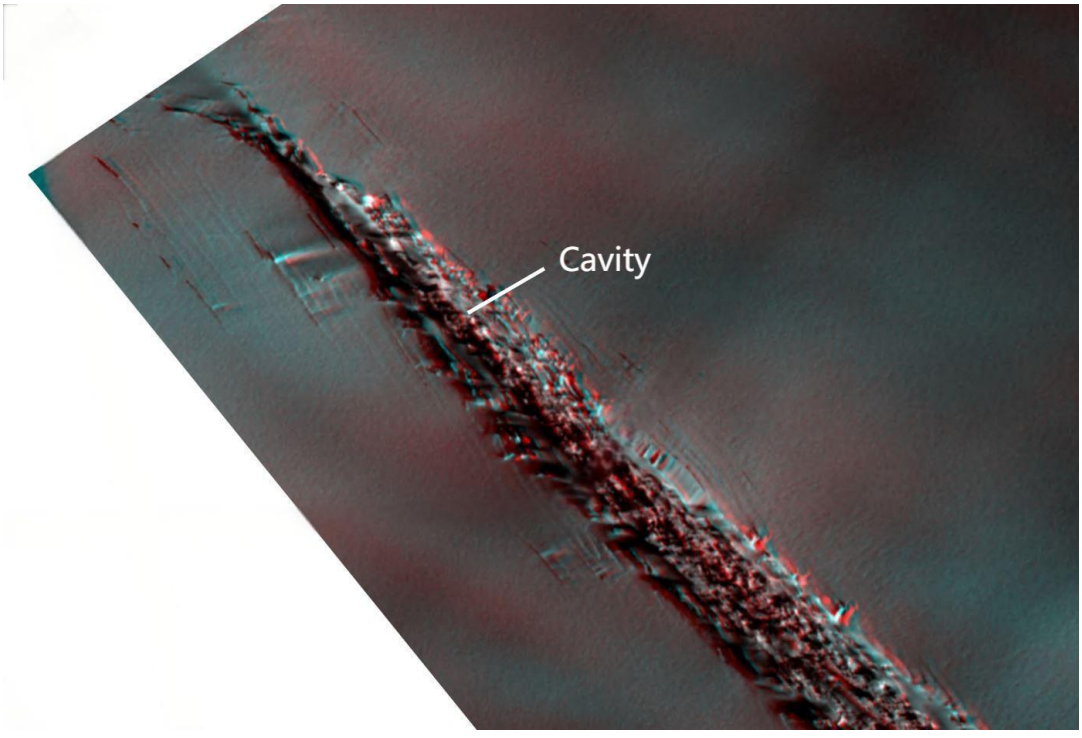

Figure A1. Anaglyph stereo pair of 2014 ZY-3 satellite images showing cavities close to the western tip of rift T1.

Table A1. Bias corrections (dX^k, dY^k, dZ^k) estimated for 15 sub-DEMs, ordered from Berkner Island to Coats Land, for the REMA DEMs of 2020-2021.

DEM^k	$dX^k \pm \sigma_{dX}$ (m)	$dY^k \pm \sigma_{dY}$ (m)	$dZ^k \pm \sigma_{dZ}$ (m)
1	1.96±1.72	-1.91±2.36	-3.92±0.13
2	-4.55±1.69	2.30±2.32	-1.02±0.14
3	-0.19±1.74	-0.80±2.39	-2.85±0.15
4	4.74±2.23	2.65±3.06	0.65±0.19
5	1.92±1.83	-3.03±2.51	-0.24±0.17
6	6.76±2.19	-5.14±3.01	-1.22±0.18
7	-3.82±3.06	5.96±4.20	0.14±0.26
8	-1.16±3.33	2.49±4.57	-1.30±0.28
9	-3.62±2.89	5.93±3.98	2.06±0.21
10	5.34±2.15	-6.17±2.96	-0.73±0.16

https://doi.org/10.5194/egusphere-2025-175
Preprint. Discussion started: 7 February 2025

11	0.55±1.69	-0.29±2.33	-11.01±0.13
12	-1.34±2.62	3.24±3.60	-1.72±0.20
13	-1.38±3.05	5.25±4.19	1.15±0.24
14	-0.59±2.54	2.98±3.49	2.20±0.20
15	0.62±1.49	-1.59±2.05	-1.84±0.11

Table A2. Information of images used for ZY-3 DEM reconstruction and REMA sub-DEMs (Howat et al., 2022).

DEM type	DEM^k	Time of image 1	Time of image 2	Time of image 3
ZY-3 DEM	-	2014/02/28 18:34:23	2014/02/28 18:34:54	2014/02/28 18:35:25
DEM type	DEM^k	ID of sub-DEM	Time of image 1	Time of image 2
REMA DEMs (2016-2017)	1	SETSM_s2s041_WV01_20161031_10200100560C2900_1020010057847400_2m_lsf_seg1	2016/10/31 06:55:50	2016/10/31 06:54:45
	2	SETSM_s2s041_WV03_20170104_10400100262E6300_10400100277D2F00_2m_lsf_seg1	2017/01/04 03:31:27	2017/01/04 03:30:17
	3	SETSM_s2s041_WV01_20161219_1020010058C54700_1020010057729D00_2m_lsf_seg1	2016/12/19 13:55:22	2016/12/19 13:56:21
	4	SETSM_s2s041_WV01_20161220_102001005AC45800_1020010058D62800_2m_lsf_seg1	2016/12/20 07:19:42	2016/12/20 07:20:36
	5	SETSM_s2s041_WV02_20161006_103001005E9F9E00_103001005D8A5100_2m_lsf_seg1	2016/10/06 11:11:37	2016/10/06 11:10:09
	6	SETSM_s2s041_WV02_20161219_10300100615A4D00_1030010062336300_2m_lsf_seg1	2016/12/19 08:59:46	2016/12/19 09:01:26
	7	SETSM_s2s041_WV01_20161219_1020010057514C00_102001005A46ED00_2m_lsf_seg1	2016/12/19 13:56:00	2016/12/19 13:54:55
	8	SETSM_s2s041_WV01_20170104_10200100594C1300_102001005ACFFC00_2m_lsf_seg1	2017/01/04 14:21:20	2017/01/04 14:20:11
	9	SETSM_s2s041_WV01_20161025_1020010056B75500_102001005814FB00_2m_lsf_seg1	2016/10/25 07:33:35	2016/10/25 07:32:32
	10	SETSM_s2s041_WV01_20161025_1020010055CA2A00_102001005658D200_2m_lsf_seg1	2016/10/25 07:33:55	2016/10/25 07:32:52
	11	SETSM_s2s041_WV02_20161212_1030010061560200_10300100614D0D00_2m_lsf_seg1	2016/12/12 03:23:10	2016/12/12 03:22:00

https://doi.org/10.5194/egusphere-2025-175
Preprint. Discussion started: 7 February 2025

	12	SETSM_s2s041_WV02_20161220_10300100633CF200_1030010062317900_2m_lsf_seg1	2016/12/20 05:07:25	2016/12/20 05:05:43
	13	SETSM_s2s041_WV02_20161004_103001005E897400_103001005E7A4B00_2m_lsf_seg1	2016/10/4 10:43:18	2016/10/4 10:45:21
	14	SETSM_s2s041_WV01_20161031_1020010057D5DD00_1020010057C58900_2m_lsf_seg1	2016/10/31 06:55:20	2016/10/31 06:54:15
REMA DEMs (2020-2021)	1	SETSM_s2s041_WV01_20210313_10200100A22EED00_10200100A41A1C00_2m_lsf_seg1	2021/03/13 14:29:27	2021/03/13 14:28:34
	2	SETSM_s2s041_WV01_20210313_10200100A4D4E000_10200100A4DAC200_2m_lsf_seg1	2021/03/13 14:28:17	2021/03/13 14:29:08
	3	SETSM_s2s041_WV01_20210126_10200100A3E1F100_10200100A6209000_2m_lsf_seg1	2021/01/26 14:01:59	2021/01/26 14:02:49
	4	SETSM_s2s041_WV01_20210116_10200100A3347F00_10200100A6DCA900_2m_lsf_seg1	2021/01/16 06:48:32	2021/01/16 06:49:26
	5	SETSM_s2s041_WV01_20210126_10200100A0336A00_10200100A3CAE800_2m_lsf_seg1	2021/01/26 14:01:37	2021/01/26 14:02:26
	6	SETSM_s2s041_WV02_20210117_10300100B354E500_10300100B4CB5400_2m_lsf_seg1	2021/01/17 11:16:55	2021/01/17 11:18:08
	7	SETSM_s2s041_WV02_20210221_10300100B2BA9B00_10300100B3853900_2m_lsf_seg1	2021/02/21 08:08:54	2021/02/21 08:07:50
	8	SETSM_s2s041_WV01_20210202_10200100A0839200_10200100A67B9000_2m_lsf_seg1	2021/02/02 13:00:47	2021/02/02 13:01:35
	9	SETSM_s2s041_WV02_20210203_10300100B33FB700_10300100B3535000_2m_lsf_seg1	2021/02/03 05:54:34	2021/02/03 05:53:18
	10	SETSM_s2s041_WV02_20210126_10300100B37B2C00_10300100B4999A00_2m_lsf_seg1	2021/01/26 09:05:41	2021/01/26 09:06:49
	11	SETSM_s2s041_WV02_20210203_10300100B409A800_10300100B4AEC000_2m_lsf_seg1	2021/02/03 10:51:17	2021/02/03 10:49:46
	12	SETSM_s2s041_WV01_20210122_10200100A2B85700_10200100A3D3D700_2m_lsf_seg1	2021/01/22 07:42:53	2021/01/22 07:43:45
	13	SETSM_s2s041_WV01_20201109_102001009EC56300_10200100A1685C00_2m_lsf_seg1	2020/11/09 06:48:36	2020/11/09 06:49:26
	14	SETSM_s2s041_WV02_20201003_10300100AE149700_10300100AE656F00_2m_lsf_seg1	2020/10/03 09:45:56	2020/10/03 09:46:59
	15	SETSM_s2s041_WV01_20200923_102001009B59CF00_102001009C2DFD00_2m_lsf_seg1	2020/09/23 13:06:20	2020/09/23 13:05:24

https://doi.org/10.5194/egusphere-2025-175
Preprint. Discussion started: 7 February 2025

Table A3. Heights of rift lips measured on the land-ward (L) side and sea-ward (S) side, and their difference (S-L) at each transect along the centerline of Rift T1 (REMA DEMs of 2016-2017).

Transect ID from west tip to east tip (1 km separation)	Land-ward lip height (L) (m)	Sea-ward lip height (S) (m)	Difference (S-L) (m)
1	1.06	1.55	0.49
2	4.68	5.37	0.69
3	4.19	6.45	2.26
4	6.31	4.29	-2.02
5	7.88	4.09	-3.79
6	3.19	2.73	-0.46
7	2.24	2.37	0.13
8	2.62	2.90	0.28
9	1.85	1.79	-0.06
10	1.48	2.29	0.81
11	1.07	1.97	0.90
12	1.23	2.52	1.29
13	1.96	3.80	1.84
14	1.84	3.98	2.14
15	1.91	3.03	1.12
16	2.06	2.68	0.62
17	2.02	2.48	0.46
18	1.71	2.16	0.45
19	2.09	2.60	0.51
20	1.47	2.23	0.76
21	1.58	2.10	0.52
22	1.65	2.37	0.72
23	1.48	2.41	0.93
24	1.01	1.63	0.62
25	1.02	2.02	1.00
26	0.96	1.96	1.00
27	1.62	1.86	0.24

https://doi.org/10.5194/egusphere-2025-175
Preprint. Discussion started: 7 February 2025

28	2.34	1.77	-0.57
29	1.76	3.67	1.91
30	3.32	5.06	1.74
31	2.28	2.95	0.67
32	2.91	3.02	0.11
33	3.14	3.86	0.72
34	2.32	3.73	1.41
35	3.18	6.26	3.08
36	1.71	4.25	2.54
37	1.19	3.66	2.47
38	1.00	3.65	2.65
39	2.58	2.33	-0.25
40	2.25	1.16	-1.09
41	2.24	1.19	-1.05
42	1.65	1.39	-0.26
43	1.72	2.68	0.96
44	1.79	1.67	-0.12
45	3.32	2.16	-1.16
46	3.39	2.97	-0.42
47	2.90	2.84	-0.06
48	3.03	4.77	1.74
49	2.71	3.87	1.16

330

Data availability. REMA DEMs used in this study are available at https://www.pgc.umn.edu/data/rema/ (last access: December 17, 2024) (Howat et al., 2019). ITS_LIVE ice flow velocity maps are at https://its-live.jpl.nasa.gov/ (last access: January 11, 2024) (Gardner et al., 2019).

335

https://doi.org/10.5194/egusphere-2025-175
Preprint. Discussion started: 7 February 2025

Author contributions. RL led the study and designed the MDAM system. MX programmed and implemented the model. ZL performed accuracy verification. RL, MX, and MS were involved in data analysis and presentation. RL, MS, LA, and GQ edited the manuscript.

Competing interests. The contact author has declared that neither they nor their co-authors have any competing interests.

Acknowledgements. We thank the United States Geological Survey (USGS) for the Landsat images, and the Chinese Ministry of Natural Resources for the ZY-3 images. The WorldView images are purchased from DigitalGlobe.

Financial support. This research has been supported by the National Natural Science Foundation of China (Grant No. 42394131), the National Key R&D Program of China (Grant No. 2024YFF0808302), and the Fundamental Research Funds for the Central Universities.

References

Adusumilli, S., Fricker, H. A., Medley, B., Padman, L., and Siegfried, M. R.: Interannual variations in meltwater input to the Southern Ocean from Antarctic ice shelves, Nat. Geosci., 13, 616-620, 10.1038/s41561-020-0616-z, 2020.

Alley, R. B., Cuffey, K. M., Bassis, J. N., Alley, K. E., Wang, S., Parizek, B. R., Anandakrishnan, S., Christianson, K., and DeConto, R. M.: Iceberg Calving: Regimes and Transitions, Annual Review of Earth and Planetary Sciences, 51, 189-215, 10.1146/annurev-earth-032320-110916, 2023.

Allison, I., Alley, R. B., Fricker, H. A., Thomas, R. H., and Warner, R. C.: Ice sheet mass balance and sea level, Antarctic Sci., 21, 413-426, 10.1017/S0954102009990137, 2009.

Anderson, N. T. and Marchisio, G. B.: WorldView-2 and the evolution of the DigitalGlobe remote sensing satellite constellation: introductory paper for the special session on WorldView-2, in: Algorithms and Technologies for Multispectral, Hyperspectral, and Ultraspectral Imagery XVIII, Algorithms and Technologies for Multispectral, Hyperspectral, and Ultraspectral Imagery XVIII, 2012/05/14, 166-180, 10.1117/12.919756, 2012.

Bindschadler, R., Vornberger, P., Fleming, A., Fox, A., Mullins, J., Binnie, D., Paulsen, S. J., Granneman, B., and Gorodetzky, D.: The Landsat image mosaic of Antarctica, Remote Sens. Environ., 112, 4214-4226, 10.1016/j.rse.2008.07.006, 2008.

Brunt, K. M., Neumann, T. A., and Smith, B. E.: Assessment of ICESat-2 Ice Sheet Surface Heights, Based on Comparisons Over the Interior of the Antarctic Ice Sheet, Geophys. Res. Lett., 46, 13072-13078, 10.1029/2019GL084886, 2019.

Cassotto, R. K., Burton, J. C., Amundson, J. M., Fahnestock, M. A., and Truffer, M.: Granular decoherence precedes ice mélange failure and glacier calving at Jakobshavn Isbræ, Nat. Geosci., 14, 417-422, 2021.

Depoorter, M. A., Bamber, J. L., Griggs, J. A., Lenaerts, J. T. M., Ligtenberg, S. R. M., van den Broeke, M. R., and Moholdt, G.: Calving fluxes and basal melt rates of Antarctic ice shelves, Nature, 502, 89-92, 10.1038/nature12567, 2013.

https://doi.org/10.5194/egusphere-2025-175
Preprint. Discussion started: 7 February 2025

DiMarzio, J., Brenner, A., Schutz, R., Shuman, C. A., and Zwally, H. J.: GLAS/ICESat 500 m laser altimetry digital elevation model of Antarctica, National Snow and Ice Data Center, 10.5067/K2IMI0L24BRJ, 2007.

Feng, T., Li, Y., Wang, K., Qiao, G., Cheng, Y., Yuan, X., Luo, S., and Li, R.: A hierarchical network densification approach for reconstruction of historical ice velocity fields in East Antarctica, J. Glaciol., 1-20, 2022.

Ferrigno, J. G. and Gould, W. G.: Substantial changes in the coastline of Antarctica revealed by satellite imagery, Polar Record, 23, 577-583, 10.1017/S003224740000807X, 1987.

Francis, D., Mattingly, K. S., Lhermitte, S., Temimi, M., and Heil, P.: Atmospheric extremes caused high oceanward sea surface slope triggering the biggest calving event in more than 50 years at the Amery Ice Shelf, The Cryosphere, 15, 2147-2165, 2021.

Fricker, H. A., Young, N. W., Coleman, R., Bassis, J. N., and Minster, J.-B.: Multi-year monitoring of rift propagation on the Amery Ice Shelf, East Antarctica, Geophys. Res. Lett., 32, 10.1029/2004GL021036, 2005.

Gardner, A. S., Fahnestock, M. A., and Scambos, T. A.: MEaSUREs ITS_LIVE Landsat Image-Pair Glacier and Ice Sheet Surface Velocities, Version 1, 10.5067/IMR9D3PEI28U., 2019.

Greene, C. A., Gardner, A. S., Schlegel, N.-J., and Fraser, A. D.: Antarctic calving loss rivals ice-shelf thinning, Nature, 609, 948-953, 10.1038/s41586-022-05037-w, 2022.

Grosfeld, K., Schröder, M., Fahrbach, E., Gerdes, R., and Mackensen, A.: How iceberg calving and grounding change the circulation and hydrography in the Filchner Ice Shelf-Ocean System, J. Geophys. Res. Oceans, 106, 9039-9055, 10.1029/2000JC000601, 2001.

Howat, I. M., Porter, C., Smith, B. E., Noh, M.-J., and Morin, P.: The reference elevation model of Antarctica, The Cryosphere, 13, 665-674, 2019.

Howat, I., Porter, C., Noh, M.-J., Husby, E., Khuvis, S., Danish, E., Tomko, K., Gardiner, J., Negrete, A., Yadav, B., Klassen, J., Kelleher, C., Cloutier, M., Bakker, J., Enos, J., Arnold, G., Bauer, G., and Morin, P.: The Reference Elevation Model of Antarctica - Strips, Version 4.1 (V1), Harvard Dataverse, doi/10.7910/DVN/X7NDNY, 2022.

Hulbe, C. L., LeDoux, C., and Cruikshank, K.: Propagation of long fractures in the Ronne Ice Shelf, Antarctica, investigated using a numerical model of fracture propagation, J. Glaciol., 56, 459-472, 10.3189/002214310792447743, 2010.

Jacobs, S. S., Helmer, H. H., Doake, C. S. M., Jenkins, A., and Frolich, R. M.: Melting of ice shelves and the mass balance of Antarctica, J. Glaciol., 38, 375-387, 10.3189/S0022143000002252, 1992.

Joughin, I. and MacAyeal, D. R.: Calving of large tabular icebergs from ice shelf rift systems, Geophys. Res. Lett., 32, 10.1029/2004GL020978, 2005.

King, E. C.: Observations of a rift in the Ronne Ice Shelf, Antarctica, J. Glaciol., 40, 187-189, 10.3189/S0022143000003968, 1994.

King, M. A., Padman, L., Nicholls, K., Clarke, P. J., Gudmundsson, G. H., Kulessa, B., and Shepherd, A.: Ocean tides in the Weddell Sea: New observations on the Filchner-Ronne and Larsen C ice shelves and model validation, J. Geophys. Res. Oceans, 116, 10.1029/2011JC006949, 2011.

https://doi.org/10.5194/egusphere-2025-175
Preprint. Discussion started: 7 February 2025

Larour, E., Rignot, E., and Aubry, D.: Modelling of rift propagation on Ronne Ice Shelf, Antarctica, and sensitivity to climate change, Geophys. Res. Lett., 31, 10.1029/2004GL020077, 2004.

Larour, E., Rignot, E., Poinelli, M., and Scheuchl, B.: Physical processes controlling the rifting of Larsen C Ice Shelf, Antarctica, prior to the calving of iceberg A68, Proceedings of the National Academy of Sciences, 118, e2105080118, 2021.

Li, R.: Potential of high-resolution satellite imagery for national mapping products, Photogrammetric Engineering and Remote Sensing, 64, 1165-1170, 1998.

Li, R., Xiao, H., Liu, S., and Tong, X.: A Systematic Study of the Fracturing of Ronne - Filchner Ice Shelf, Antarctica,Using Multisource Satellite Data from 2001 to 2016, The Cryosphere Discussions, 1-38, 2017.

Li, R., Cheng, Y., Cui, H., Xia, M., Yuan, X., Li, Z., Luo, S., and Qiao, G.: Overestimation and adjustment of Antarctic ice flow velocity fields reconstructed from historical satellite imagery, The Cryosphere, 16, 737-760, 10.5194/tc-16-737-2022, 2022.

Li, R., Li, H., Hao, T., Qiao, G., Cui, H., He, Y., Hai, G., Xie, H., Cheng, Y., and Li, B.: Assessment of ICESat-2 ice surface elevations over the Chinese Antarctic Research Expedition (CHINARE) route, East Antarctica, based on coordinated multi-sensor observations, The Cryosphere, 15, 3083-3099, 2021.

Li, R., Cheng, Y., Chang, T., Gwyther, D. E., Forbes, M., An, L., Xia, M., Yuan, X., Qiao, G., Tong, X., and Ye, W.: Satellite record reveals 1960s acceleration of Totten Ice Shelf in East Antarctica, Nat. Commun., 14, 4061, 10.1038/s41467-023-39588-x, 2023a.

Li, T., Hu, Y., Liu, B., Jiang, L., Wang, H., and Shen, X.: Co-registration and residual correction of digital elevation models: a comparative study, The Cryosphere, 17, 5299-5316, 10.5194/tc-17-5299-2023, 2023b.

Liu, H., Jezek, K., Li, B., and Zhao, Z.: Radarsat Antarctic Mapping Project digital elevation model version 2, Radarsat Antarctic Mapping Project digital elevation model version 2, 2001.

Liu, Y., Moore, J. C., Cheng, X., Gladstone, R. M., Bassis, J. N., Liu, H., Wen, J., and Hui, F.: Ocean-driven thinning enhances iceberg calving and retreat of Antarctic ice shelves, Proceedings of the National Academy of Sciences, 112, 3263-3268, 2015.

Lv, D., Cheng, Y., Xiao, H., and Hai, G.: A Framework for Fracture Extraction Under Glaciological Property-Based Constraints: Scientific Application on the Filchner–Ronne Ice Shelf of Antarctica, Earth and Space Science, 9, e2022EA002293, 10.1029/2022EA002293, 2022.

Magruder, L. A., Brunt, K. M., and Alonzo, M.: Early ICESat-2 on-orbit Geolocation Validation Using Ground-Based Corner Cube Retro-Reflectors, Remote Sensing, 12, 3653, 10.3390/rs12213653, 2020.

Magruder, L., Neumann, T., and Kurtz, N.: ICESat-2 Early Mission Synopsis and Observatory Performance, Earth and Space Science, 8, e2020EA001555, 10.1029/2020EA001555, 2021.

Markus, T., Neumann, T., Martino, A., Abdalati, W., Brunt, K., Csatho, B., Farrell, S., Fricker, H., Gardner, A., Harding, D., Jasinski, M., Kwok, R., Magruder, L., Lubin, D., Luthcke, S., Morison, J., Nelson, R., Neuenschwander, A., Palm, S., Popescu, S., Shum, C., Schutz, B. E., Smith, B., Yang, Y., and Zwally, J.: The Ice, Cloud, and land Elevation Satellite-2 (ICESat-2): Science requirements, concept, and implementation, Remote Sens. Environ., 190, 260-273, 10.1016/j.rse.2016.12.029, 2017.

https://doi.org/10.5194/egusphere-2025-175
Preprint. Discussion started: 7 February 2025

McGlone, J., Mikhail, E., Bethel, J., and Mullen, R.: Manual of photogrammetry, 5th ed., American Society for Photogrammetry and Remote Sensing2004.

Moctezuma-Flores, M., Parmiggiani, F., and Guerrieri, L.: Tracking of the huge Antarctic iceberg A-76, Remote Sensing Letters, 14, 10-20, 10.1080/2150704X.2022.2152292, 2023.

Morlighem, M., Rignot, E., Binder, T., Blankenship, D., Drews, R., Eagles, G., Eisen, O., Ferraccioli, F., Forsberg, R., and Fretwell, P.: Deep glacial troughs and stabilizing ridges unveiled beneath the margins of the Antarctic ice sheet, Nat. Geosci., 13, 132-137, 10.1038/s41561-019-0510-8, 2020.

Neuburg, H. A. C., Thiel, E., Walker, P. T., Behrendt, J. C., and Aughenbaugh, N. B.: The Filchner Ice Shelf, Annals of the Association of American Geographers, 49, 110-119, 10.1111/j.1467-8306.1959.tb01603.x, 1959.

Noh, M.-J. and Howat, I. M.: Automated stereo-photogrammetric DEM generation at high latitudes: Surface Extraction with TIN-based Search-space Minimization (SETSM) validation and demonstration over glaciated regions, GIScience & Remote Sensing, 52, 198-217, 10.1080/15481603.2015.1008621, 2015.

Nuth, C. and Kääb, A.: Co-registration and bias corrections of satellite elevation data sets for quantifying glacier thickness change, The Cryosphere, 5, 271-290, 2011.

Otosaka, I. N., Shepherd, A., Ivins, E. R., Schlegel, N.-J., Amory, C., van den Broeke, M. R., Horwath, M., Joughin, I., King, M. D., Krinner, G., Nowicki, S., Payne, A. J., Rignot, E., Scambos, T., Simon, K. M., Smith, B. E., Sørensen, L. S., Velicogna, I., Whitehouse, P. L., A, G., Agosta, C., Ahlstrøm, A. P., Blazquez, A., Colgan, W., Engdahl, M. E., Fettweis, X., Forsberg, R., Gallée, H., Gardner, A., Gilbert, L., Gourmelen, N., Groh, A., Gunter, B. C., Harig, C., Helm, V., Khan, S. A., Kittel, C., Konrad, H., Langen, P. L., Lecavalier, B. S., Liang, C.-C., Loomis, B. D., McMillan, M., Melini, D., Mernild, S. H., Mottram, R., Mouginot, J., Nilsson, J., Noël, B., Pattle, M. E., Peltier, W. R., Pie, N., Roca, M., Sasgen, I., Save, H. V., Seo, K.-W., Scheuchl, B., Schrama, E. J. O., Schröder, L., Simonsen, S. B., Slater, T., Spada, G., Sutterley, T. C., Vishwakarma, B. D., van Wessem, J. M., Wiese, D., van der Wal, W., and Wouters, B.: Mass balance of the Greenland and Antarctic ice sheets from 1992 to 2020, Earth Syst. Sci. Data, 15, 1597-1616, 10.5194/essd-15-1597-2023, 2023.

Padman, L., Erofeeva, S. Y., and Fricker, H. A.: Improving Antarctic tide models by assimilation of ICESat laser altimetry over ice shelves, Geophys. Res. Lett., 35, 10.1029/2008GL035592, 2008.

Rignot, E. and MacAyeal, D. R.: Ice-shelf dynamics near the front of the Filchner—Ronne Ice Shelf, Antarctica, revealed by SAR interferometry, J. Glaciol., 44, 405-418, 10.3189/S0022143000002732, 1998.

Rignot, E., Mouginot, J., and Scheuchl, B.: Ice flow of the Antarctic ice sheet, Science, 333, 1427-1430, 10.1126/science.1208336, 2011.

Rignot, E., Mouginot, J., Scheuchl, B., Van Den Broeke, M., Van Wessem, M. J., and Morlighem, M.: Four decades of Antarctic Ice Sheet mass balance from 1979–2017, Proceedings of the National Academy of Sciences, 116, 1095-1103, 2019.

Shean, D. E., Joughin, I. R., Dutrieux, P., Smith, B. E., and Berthier, E.: Ice shelf basal melt rates from a high-resolution digital elevation model (DEM) record for Pine Island Glacier, Antarctica, The Cryosphere, 13, 2633-2656, 2019.

https://doi.org/10.5194/egusphere-2025-175
Preprint. Discussion started: 7 February 2025

Shen, X., Ke, C.-Q., Fan, Y., and Drolma, L.: A new digital elevation model (DEM) dataset of the entire Antarctic continent derived from ICESat-2, Earth Syst. Sci. Data, 14, 3075-3089, 2022.

Slater, T., Shepherd, A., McMillan, M., Muir, A., Gilbert, L., Hogg, A. E., Konrad, H., and Parrinello, T.: A new digital elevation model of Antarctica derived from CryoSat-2 altimetry, The Cryosphere, 12, 1551-1562, 2018.

Smith, B., Fricker, H. A., Gardner, A. S., Medley, B., Nilsson, J., Paolo, F. S., Holschuh, N., Adusumilli, S., Brunt, K., Csatho, B., Harbeck, K., Markus, T., Neumann, T., Siegfried, M. R., and Zwally, H. J.: Pervasive ice sheet mass loss reflects competing ocean and atmosphere processes, Science, 368, 1239-1242, 10.1126/science.aaz5845, 2020.

Tachikawa, T., Hato, M., Kaku, M., and Iwasaki, A.: Characteristics of ASTER GDEM version 2, 2011 IEEE international geoscience and remote sensing symposium, Vancouver, BC, Canada, 3657-3660,

Thompson, S. S., Cook, S., Kulessa, B., Winberry, J. P., Fraser, A. D., and Galton-Fenzi, B. K.: Comparing satellite and helicopter-based methods for observing crevasses, application in East Antarctica, Cold Regions Science and Technology, 178, 103128, 10.1016/j.coldregions.2020.103128, 2020.

Walker, C. and Gardner, A.: Evolution of ice shelf rifts: Implications for formation mechanics and morphological controls, Earth Planet. Sci. Lett., 526, 115764, 2019.

Walker, C. C., Becker, M. K., and Fricker, H. A.: A High Resolution, Three-Dimensional View of the D-28 Calving Event From Amery Ice Shelf With ICESat-2 and Satellite Imagery, Geophys. Res. Lett., 48, e2020GL091200, 10.1029/2020GL091200, 2021.

Wang, S., Liu, H., Jezek, K., Alley, R. B., Wang, L., Alexander, P., and Huang, Y.: Controls on Larsen C Ice Shelf Retreat From a 60-Year Satellite Data Record, J. Geophys. Res.- Earth Surf., 127, e2021JF006346, 10.1029/2021JF006346, 2022.

Wang, T., Zhang, G., Li, D., Tang, X., Jiang, Y., Pan, H., Zhu, X., and Fang, C.: Geometric Accuracy Validation for ZY-3 Satellite Imagery, IEEE Geosci. Remote Sens. Lett., 11, 1168-1171, 10.1109/LGRS.2013.2288918, 2014.

Wessel, B., Huber, M., Wohlfart, C., Bertram, A., Osterkamp, N., Marschalk, U., Gruber, A., Reuß, F., Abdullahi, S., and Georg, I.: TanDEM-X PolarDEM 90 m of Antarctica: Generation and error characterization, The Cryosphere, 15, 5241-5260, 2021.

Williams, R. M., Ray, L. E., Lever, J. H., and Burzynski, A. M.: Crevasse Detection in Ice Sheets Using Ground Penetrating Radar and Machine Learning, IEEE J. Sel. Topics Appl. Earth Observ. Remote Sens., 7, 4836-4848, 10.1109/JSTARS.2014.2332872, 2014.

Zinck, A.-S. P., Wouters, B., Lambert, E., and Lhermitte, S.: Unveiling spatial variability within the Dotson Melt Channel through high-resolution basal melt rates from the Reference Elevation Model of Antarctica, The Cryosphere, 17, 3785-3801, 10.5194/tc-17-3785-2023, 2023.